

Observations of Orion Source I Disk and Outflow Interface

MELVYN WRIGHT,¹ RICHARD PLAMBECK,¹ TOMOYA HIROTA,² ADAM GINSBURG,³ BRETT MCGUIRE,³
JOHN BALLY,⁴ AND CIRIACO GODDI⁵

¹*Radio Astronomy Lab, University of California, 501 Campbell Hall, Berkeley CA 94720-3441, USA*

²*Mizusawa VLBI Observatory, National Astronomical Observatory of Japan, Osawa 2-21-1, Mitaka, Tokyo 181-8588, Japan*

³*National Radio Astronomy Observatory, Charlottesville, VA 22903, USA*

⁴*CASA, University of Colorado, 389-UCB, Boulder, CO 80309, USA*

⁵*Leiden Observatory, Leiden University, P.O. Box 9513, 2300 RA Leiden, The Netherlands*

ABSTRACT

We imaged the continuum and molecular line emission from Orion Source I (SrcI) with up to 30 mas (12 AU) resolution at 43, 99, 223, and 340 GHz in an attempt to probe the structure and chemistry of the circumstellar disk and bipolar outflow associated with this high mass protostar. The continuum spectral index ranges from ~ 2 along the midplane of the disk to ~ 3 along the edges, consistent with dust that is optically thick in the midplane but becomes optically thin at the periphery. Salt (NaCl) emission is visible where the dust is optically thin; it provides a unique tracer of the velocity field within the disk. All other molecules that we have mapped – H₂O, AlO, SiO, SiS, SO, and SO₂ – appear to originate primarily in the bipolar outflow. The base of the outflow is corotating with the disk. SiS shows a filamentary structure that is most prominent along the edges of the outflow. The molecular distributions suggest that Si and Al released from dust grains in the disk react with oxygen derived from H₂O to form SiO and AlO, and with SO and SO₂ to form SiS.

Keywords: radio continuum: stars — radio lines: stars — stars: individual (Orion source I)

1. INTRODUCTION

The Kleinmann-Low Nebula in Orion, at a distance 415 pc (Menten et al. 2007; Kim et al. 2008; Kounkel et al. 2018), is the nearest interstellar cloud in which massive ($M > 8 M_{\odot}$) stars are forming. The two most massive stars in this region, Source I (SrcI) and the Becklin-Neugebauer Object (BN), appear to be recoiling from one another at 35-40 km s⁻¹ (Rodríguez et al. 2005; Gómez et al. 2008; Goddi et al. 2011b), suggesting that they were ejected from a multiple system via dynamical decay approx-

imately 500 years ago (Bally et al. 2017). SrcI has a mass $\sim 15 M_{\odot}$ (Ginsburg et al. 2018), with a rotating accretion disk and a molecular outflow that is prominent in SiO. The disk around SrcI has been well studied as it is the closest known disk around a high mass protostar (Hirota et al. 2014; Plambeck & Wright 2016; Ginsburg et al. 2018); it is associated with SiO and H₂O masers (Reid et al. 2007; Goddi et al. 2009; Plambeck et al. 2009; Matthews et al. 2010; Goddi et al. 2011b; Niederhofer et al. 2012; Greenhill et al. 2013). Recently dozens of spectral lines of NaCl and KCl were

identified in this disk (Ginsburg et al. 2019). The rich chemistry of SrcI’s disk and outflow raises the question of whether this source is a paradigm for high-mass star formation, or an anomaly born in the unique environment created by the SrcI/BN interaction and associated explosive outflow (Bally et al. 2017).

In this paper, we present high resolution images of SrcI that were made from JVLA and ALMA data at 43, 99, 223, and 340 GHz. We use continuum images with 30 mas (12 AU) resolution to probe the dust opacity across the disk. We discuss chemical pathways that can lead to the observed molecular distributions.

2. OBSERVATIONS AND DATA REDUCTION

Table 1 provides a summary of the observations, including project codes.

2.1. 43 GHz

The spectral setup for the 43 GHz JVLA observations included 16 wideband windows, each covering 116 MHz bandwidth and 58 spectral channels. The JVLA wideband setup is 64 channels covering 128 MHz; the reduction script trimmed off end channels because of analog filter rolloff. The data were self-calibrated using a strong SiO $v = 1, J = 1 - 0$ maser feature at -3.5 km s^{-1} that was observed simultaneously in a narrowband window with spectral resolution 0.3 km s^{-1} .

The wide band average with a mean frequency of 42.65 GHz and a bandwidth of 1.4 GHz excludes 4 spectral windows containing spectral line emission. We made images with the synthesized beam width of $56 \times 44 \text{ mas}$, and convolved to 30 mas and 50 mas resolution for comparison with images at 99 GHz (see below).

2.2. 99 GHz

ALMA observations at 99 GHz (Band 3; B3) on 2017 Oct 12 and 17 included 4 spectral windows, each with a bandwidth of 1.875 GHz and

960 spectral channels. The wide band average with a mean frequency of 99.275 GHz and a bandwidth of 7.5 GHz excludes channels containing spectral line emission. The data were calibrated using observatory supplied scripts. We made images with the synthesized beam width $45 \times 36 \text{ mas}$, and convolved to 30 mas and 50 mas resolution for comparison with images at 43 GHz.

2.3. 223 and 340 GHz

The 223 GHz (ALMA Band 6; B6) and 340 GHz (ALMA Band 7; B7) observations and calibration are described in Ginsburg et al. (2018). These data were not self-calibrated. The observational parameters are given in Table 1.

In order to compare the SrcI outflow with the large scale structure associated with the SrcI/BN explosion mapped in CO by Bally et al. (2017), we imaged other spectral lines that fell within the passband of these lower resolution observations (ADS/JAO.ALMA#2013.1.00546.S). The data were calibrated using the observatory-supplied CASA scripts. We made mosaic images from these data in a $30''$ field around SrcI in SO, SO₂, and SiO emission with $1.5 \times 0.9''$ angular and 2 km s^{-1} velocity resolution. We used only the ALMA 12m array data in these images to filter out the large scale structure and enhance the filamentary structures.

The MIRIAD software package (Sault et al. 1995) was used to image and analyze all the data in this paper.

3. THE SRC I DISK

We used both CLEAN and Maximum Entropy algorithms to image the JVLA and ALMA data. We convolved the continuum images to a common resolution of 30 mas and 50 mas resolution in order to make spectral index images between 43, 99, 223 and 340 GHz. Because the 43 GHz data were self-calibrated, the wideband image was spatially offset from the higher frequency

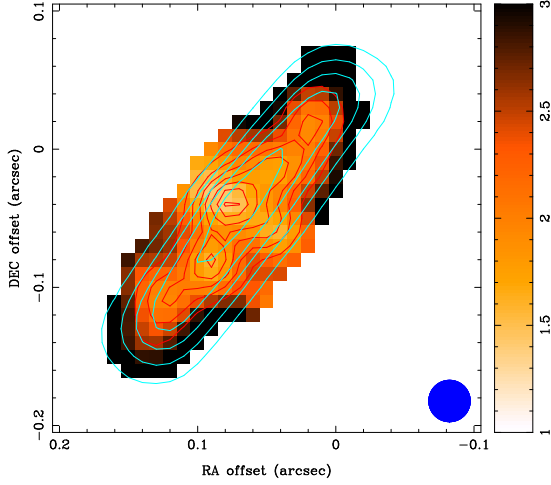


Figure 1. Spectral Index from 99 to 340 GHz. Red contour levels at 99 GHz: 200 400 600 800 1000 1200 1400 K. Blue contour levels at 340 GHz: 100 200 300 400 500 600 K. The color images shows the spectral index distribution. The 30 mas convolving beam FWHM is indicated in blue in the lower right.

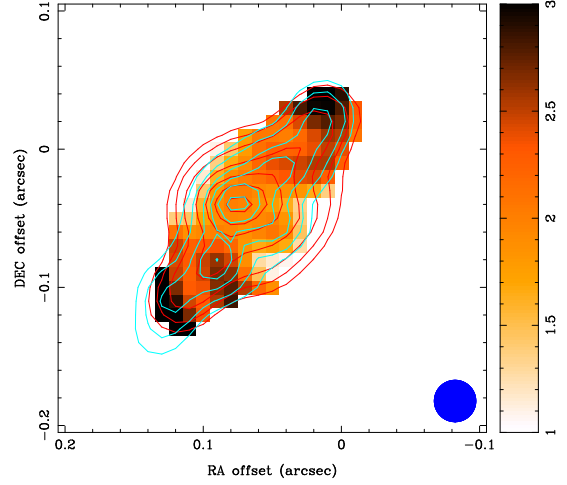


Figure 2. Spectral Index 43 GHz to 99 GHz. Red contour levels at 43 GHz: 200 400 600 800 1000 1200 1400 K. Blue contour levels at 99 GHz: 100 200 300 400 500 600 K. The color image shows the spectral index distribution. The 30 mas convolving beam FWHM is indicated in blue in the lower right.

images. We aligned the 43 GHz image with the 99 GHz image using MIRIAD task *imdiff* which finds optimum parameters in a maximum likelihood sense for making one image approximate another image. The parameters adjusted were shifts 9 mas in RA and -2 mas in DEC to an image center at RA = 05:35:14.513, DEC = -05:22:30.576 used in the following figures. The 99, 223, and 340 GHz data were not self calibrated, only the 43 GHz image position was adjusted. Src I is moving at $Dx=6.3$, $Dy=-4.2$ mas/yr (Goddi et al. 2011b). The 99, 223, and 340 GHz image data were acquired within a ~ 2 month period (see Table 1) and the offset in the images from the proper motion is less than ~ 0.4 AU.

3.1. Spectral Index Distribution

Figures 1, 2 and 3 show the spectral index computed from the ratio of continuum brightness at 340, 223, 99, and 43 GHz at 30 mas resolution. At 50 mas resolution, the same spectral index distributions are seen, convolved to the lower resolution. The RMS noise levels on

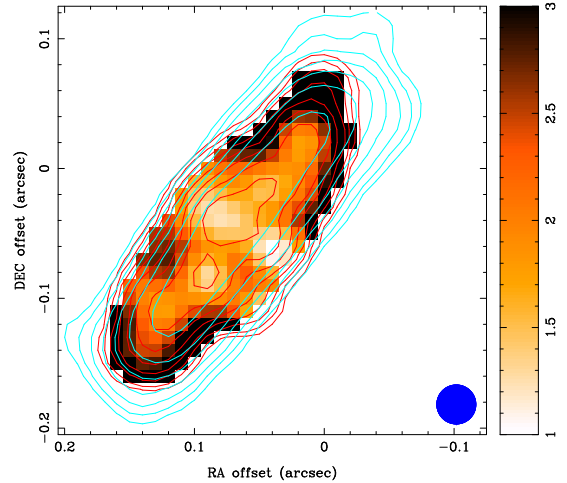


Figure 3. Spectral Index from 99 to 223 GHz. Red contour levels at 99 GHz: 5 10 20 40 80 160 320 640 K. Blue contour levels at 223 GHz: 5 10 20 40 80 160 320 640 K. The color image shows the spectral index distribution. The 30 mas convolving beam FWHM is indicated in blue in the lower right.

the continuum images are 4 K, 3 K, 7 K, and 6 K, respectively; the images were clipped at 5% of the peak for the spectral index calculation. The figures show that spectral index ~ 2

along the midplane of the disk, consistent with optically thick emission, almost certainly from dust (Plambeck & Wright 2016). The spectral index steepens to ~ 3 at the edges and ends of the disk, indicating emission from optically thin dust. In figure 2, we see that the central source is more prominent at 43 GHz, and also note the steepening of the spectral index at the ends of the disk between 43 and 99 GHz.

Uncertainties in the spectral indices are dominated by the absolute flux calibration accuracy of $\sim 10\%$ for each frequency band. A multiplicative error in the flux ratio is an additive error in the spectral index of $+0.15$ and -0.18 in the 340/99 GHz spectral index image, $+0.22$ and -0.28 in the 223/99 GHz image, and $+0.11$ and -0.13 in the 99/43 GHz image. A least squares fit from 43 to 340 GHz to the spectral index at the central position gives 1.6 ± 0.1 , whereas at the ends of the disk the fitted spectral index is 3.4 ± 0.3 . The spectral index variations across the images are significant.

3.2. Disk Structure

Ginsburg et al. (2018) fitted the observed structure of the disk from B3 and B6 ALMA continuum observations at 50 and 20 mas resolution, respectively. They determined that the disk has a length of ~ 100 AU, and vertical FWHM height of ~ 20 AU. They also detected a compact source near the center of the disk, smeared parallel to the disk major axis. The model residuals shown by Ginsburg et al. (2018) have a halo of emission at the ~ 30 K level in the B6 image that may be from optically thin dust, as it was not seen in the B3 image. This halo of emission is evident in Figure 3, where both B3 and B6 are plotted at the same logarithmic contour levels.

Table 2 summarizes the results of Gaussian fits to the disk size in our 4 continuum images. The disk major axis increases with observing frequency, which is expected as the dust optical depth increases. The minor axis is largest at 43

GHz, however, indicating that the central point source is more prominent at lower frequencies.

If we assume that the disk is circular and infinitesimally thin, we can set a lower limit on its inclination angle. The 224 and 340 GHz source sizes given in Table 2 imply that this lower limit is $78\text{-}80^\circ$.

In Figure 4 we show a Maximum Entropy image of the B7 continuum emission. The lower limit to the inclination estimated from the major and minor axes of the Maximum Entropy image is $79 \pm 1^\circ$ measured at the 400 K contour (99×19 AU), and $74 \pm 1^\circ$ measured at the 25 K contour (239×45 AU). The lowest contours at the ends of the disk suggest a flared structure, so the inclination measured at the 400 K contour is better determined. If the disk were inclined by as much as 74 or 79° , the ~ 20 AU disk thickness, would imply that the SW edge should be slightly curved. The incredibly straight SW edge in Figure 4, suggests that the inclination is closer to 90° .

A third estimate of the disk orientation can be obtained from the SiO outflow. At the highest velocities, the SiO outflow is blue-shifted to the NE, and red-shifted to the SW. This is more easily seen in Figure 1 of Plambeck et al. (2009), which maps the large scale structure of the SiO outflow. The blue-shifted emission at -13.5 km s^{-1} subtends an angle 27° at a radius ~ 1300 AU to the NE, and the red-shifted emission at 21.9 km s^{-1} subtends an angle 26° at a radius ~ 1400 AU. The red-blue asymmetry in the outflow implies that the NE edge of the disk is tipped toward us. Proper motion measurements of compact structures in the outflow could enable us to derive an inclination from the SiO outflow. Matthews et al. (2010) derive an inclination $\sim 85^\circ$ from SiO masers close to the disk.

In Figure 5, we compare Maximum Entropy images of the 340 GHz and 223 GHz continuum emission, both convolved by a 10 mas Gaus-

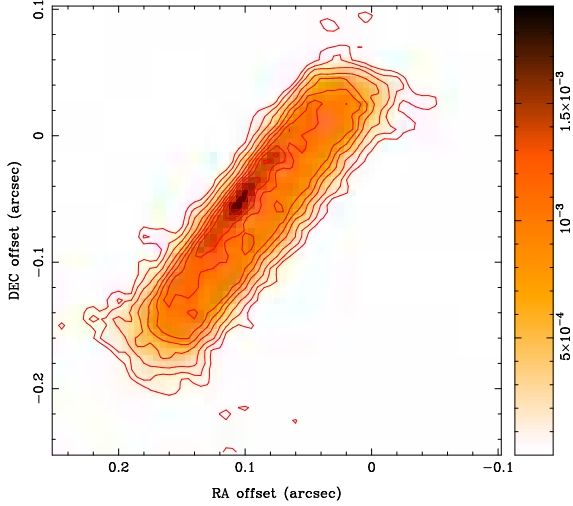


Figure 4. 340 GHz continuum emission. Maximum Entropy image with 5 mas pixels. Contours are at 25, 50, 100, 200, 300, 400, 500, 600, 700, and 800 K. The linear color scale in units Jy pixel^{-1} . (480 K mJy^{-1}). The peak brightness at the compact source is 874 K.

sian beam. As expected, the convolution reduces the gradients at the edges of the disk, which are still steeper on the NE edge than the SW edge. In both images, the brightness temperature plateau of the disk, ignoring the compact source on the NE side, is $\sim 400 \text{ K}$. The brightness falls to $\sim 200 \text{ K}$ on the 223 GHz image, where the brightness on the 340 GHz image is still $\sim 400 \text{ K}$. If we attribute this to dust emission, then the dust opacity at 223 GHz is ~ 0.7 , where the emission is still optically thick at 340 GHz. At the disk edges, the logarithmic contour levels are approximately evenly spaced, suggesting an exponential gradient in the emission. The $1/e$ scale height estimated from the gradient between 400 and 25 K at the edge of the disk at 340 GHz $\sim 2 \text{ AU}$ on the facing, NE side, to $\sim 4 \text{ AU}$ on the SW side. We may be seeing deeper into the disk on the facing, NE side where the continuum emission is brighter.

Since the disk surface layers are being torn up by the outflow as the dust grains are destroyed, however, it is likely that the spectral index of the dust emission varies through the surface lay-

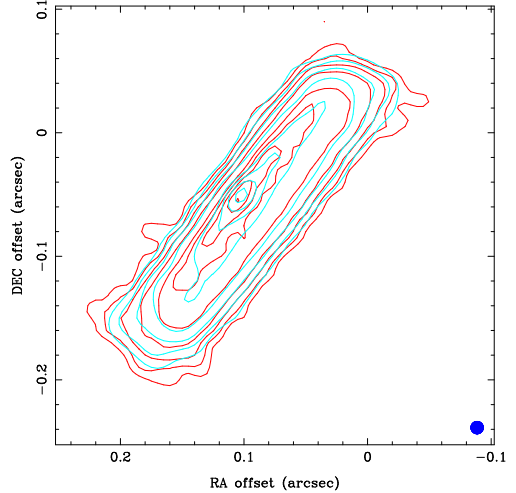


Figure 5. Comparison of the Maximum Entropy images at 340 GHz and 223 GHz convolved with a 10 mas beam shown in lower right. Contours are at 25, 50, 100, 200, 300, 400, 500, 600, 700, and 800 K.

ers, and we do not make further interpretation of the density profile of the disk surface.

3.3. Salt Emission

Figure 6 shows NaCl emission at 232.51 GHz overlaid on contours of 99 GHz and 340 GHz continuum images. Salt emission is found in the dust layer at the surface of SrcI where there is a large spectral index gradient. A gradient in the dust opacity may help to explain the discrepancy in the NaCl excitation temperatures estimated from rotationally and vibrationally excited levels (Ginsburg et al. 2019). Figure 7 shows a comparison of NaCl emission at 232.51 GHz and 335.51 GHz averaged in 5 km s^{-1} channels, overlaid on the spectral index image between 99 and 223 GHz. Both NaCl lines have peaks in the surface layers on both sides of the disk at close to the same positions. The 335 GHz NaCl $v = 1, J = 26 - 25$ line is strongly attenuated where the spectral index is less than ~ 2 . The 232 GHz NaCl $v = 1, J = 18 - 17$ line is less attenuated and shows a bridge of emission between the two peaks. The NaCl emission is brighter on the NE side of the disk which is facing towards us. This could also be because

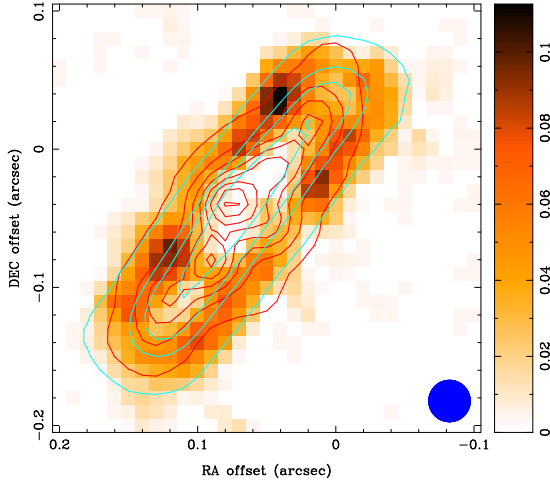


Figure 6. NaCl emission at 232.51 GHz integrated over an LSR velocity range (-30 to 30) km s^{-1} . Red contour levels at 99 GHz: 25 200 400 600 800 1000 1200 1400 K. Blue contour levels at 340 GHz: 25 200 300 400 500 600 K. The color image shows the NaCl distribution. The 30 mas convolving beam FWHM is indicated in blue in the lower right.

there is less attenuation by the disk. Thus, we suggest that the rotational temperatures, over a large range of observing frequencies, could be underestimated because of greater dust opacity at high frequencies, whereas the vibrational temperatures, over a small range of frequencies, are less affected.

4. THE SRC I OUTFLOW

4.1. H_2O

Figure 8 shows H_2O emission at 232.687 GHz overlaid on 43 GHz continuum, and spectral index images. H_2O emission extends from the surface of the SrcI disk into the outflow, and rotates with the SrcI disk. In contrast with the salt emission, the H_2O emission is more closely associated with the inner part of the disk, shown here at 43 GHz. The H_2O emission may be in part excited by radiation from the central source, and is brighter on the NE side where we see deeper into the disk. Hirota et al. (2017) present a model where the H_2O comes from the disk surface, and is driven by a magnetocentrifugal disk wind (Matthews et al. 2010; Vaidya

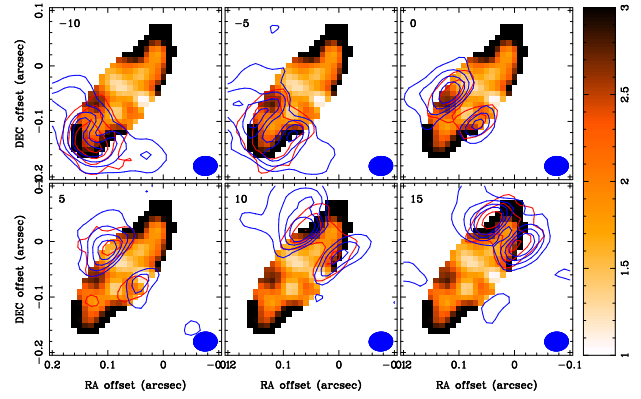


Figure 7. Comparison of NaCl emission at 232.51 GHz and 335.51 GHz averaged in 5 km s^{-1} channels, overlaid on the spectral index image. Red contours in NaCl line at 232.51 GHz: contour interval 20 K. Blue contours in NaCl line at 335 GHz: contour interval 20 K. The channel at 15 km s^{-1} is only 4.3 km s^{-1} wide to avoid contamination from adjacent spectral lines. The 30×40 mas convolving beam FWHM is indicated in blue in the lower right.

& Goddi 2013; Greenhill et al. 2013; Hirota et al. 2017).

4.2. AIO

We mapped the AIO N=6-5 line at 229.69387 GHz, and the AIO N=9-8 line at 344.4537 GHz. Figure 9 shows 229.694 GHz AIO emission overlaid on 43 GHz continuum and H_2O emission at 232.687 GHz. AIO emission is coextensive with H_2O , but the peaks are further out, and brighter on the NE side of SrcI. Since the NE side of the disk is facing towards us, we may be able to see deeper into the central regions. The distributions of AIO emission and H_2O shown here are consistent with those presented by Tachibana et al. (2019) for AIO N=13-12 and N=17-16 emission lines at 497 and 650 GHz, and H_2O at 643 GHz (Hirota et al. 2017). Tachibana et al. (2019) attribute the distribution of AIO as due to its formation at the base of the outflow, and condensation further out into the outflow. Our observations with $\sim 4\times$ higher angular resolution, suggest that

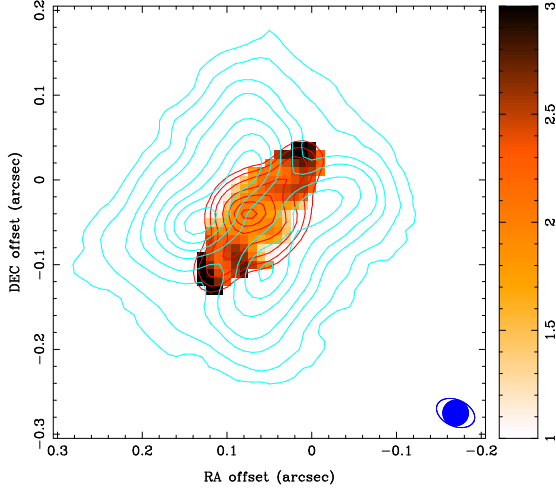


Figure 8. H₂O emission at 232.687 GHz. The color image shows the 43 to 99 GHz spectral index. Red contours show the 43 GHz continuum emission at levels: 50, 100, 200, 400, 600, 800, 1000, 1200, and 1400 K. Blue contours show the H₂O emission at 232.6867 GHz integrated over a velocity range (-50 to 50) km/s. The contour levels are 0.05, 0.1, 0.2, 0.3, 0.5, 0.7, 0.9, and $1.1 \times 15345 \text{ K km s}^{-1}$. The 30 mas convolving beam FWHM for the continuum image and spectral index image is indicated in blue filled circle. The FWHM beam for the H₂O emission was 0.05×0.03 arcsec in PA 65° shown as the open ellipse in the lower right.

AlO emission peaks downstream of the H₂O, and may be produced by grain destruction and oxidized by O released by the dissociation of H₂O, or released as AlO further out in the outflow than the H₂O emission.

4.3. SiO

The SiO masers associated with SrcI have been mapped using VLBI at 43 GHz (Kim et al. 2008; Matthews et al. 2010), and 86 GHz (Issaoun et al. 2017). The $J = 1 - 0$ and $J = 2 - 1$, $v = 1$ and $v = 2$ masers positions lie in an X pattern, with blue-shifted emission in the south and east arms, and red-shifted emission in the north and west arms. The $J = 1 - 0$ and $J = 2 - 1$ $v = 1$ and $v = 2$ masers can be interpreted as tracing a wide angle outflow arising from the surface of the almost edge on ro-

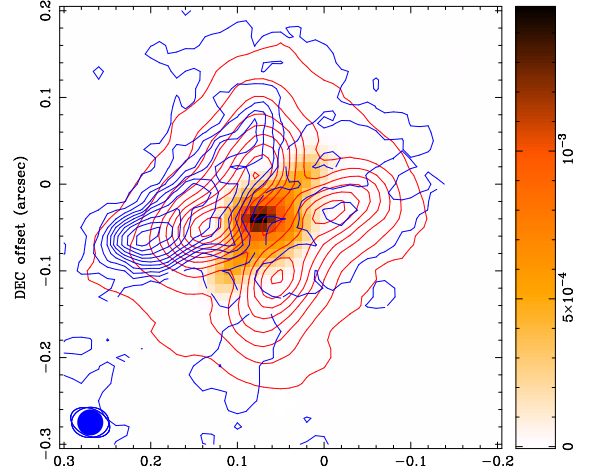


Figure 9. AlO N=6-5 emission at 229.6938725 GHz overlaid on 43 GHz continuum, and H₂O emission at 232.6867 GHz. Red contours show the H₂O emission at 232.6867 GHz integrated over a velocity range (-50 to 50) km/s. Lowest contour 933, contour interval 1866 K km s^{-1} . Blue contours show the AlO N=6-5 emission integrated over -50 to 50 km s⁻¹. Lowest contour 225, contour interval 450 K km s^{-1} . The 30 mas convolving beam FWHM for the 43 GHz continuum image is indicated in blue filled circle. The FWHM beams for the H₂O emission of 0.05×0.03 arcsec in PA 65° , and for the AlO N=6-5, 0.04×0.03 arcsec in PA -88° , are shown as the open ellipses in the lower left.

tating disk (Issaoun et al. 2017). No masers are located within a 14 AU band in PA $\sim 141^\circ$ that corresponds to the continuum emission from the disk (Matthews et al. 2010). Goddi et al. (2009) modeled the SiO maser excitation including both radiative and collisional excitation. The model predicts densities $n_{H_2} = 10^8$ to 10^{10} cm^{-3} for the $v = 1$, and 10^9 to 10^{11} cm^{-3} for the $v = 2$ transitions. The $v = 2$ transition is favored where $T_k > 2000 \text{ K}$, closer to SrcI than $v = 1$ as is observed (Kim et al. 2008; Matthews et al. 2010). Figure 10 shows SiO $v = 0$, $J = 5 - 4$ emission at 217.10498 GHz overlaid on the 43 GHz continuum and 232.69 GHz H₂O emission. The centroid positions of the $J = 2 - 1$ masers mapped using the VLBA are indicated

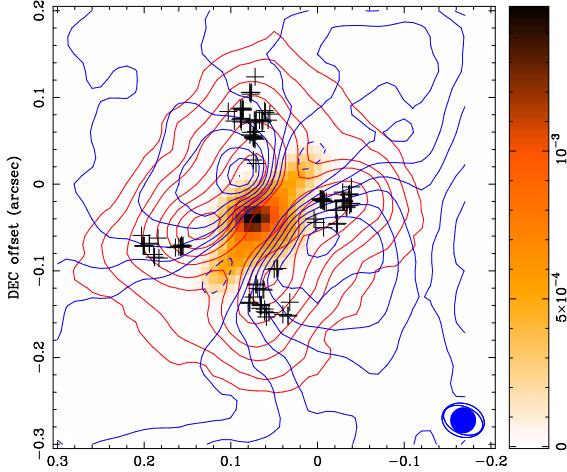


Figure 10. SiO $v = 0$ $J = 5 - 4$ emission at 217.10498 GHz overlaid on 43 GHz continuum and H₂O emission at 232.6867 GHz. The color image shows the 43GHz continuum emission Red contours show the H₂O emission at 232.6867 GHz integrated over a velocity range of -50 to 50 km s⁻¹. The contour levels are: 0.05, 0.1, 0.2, 0.3, 0.5, 0.7, 0.9, and 1.1×15345 K km s⁻¹. Blue contours show the SiO $v = 0$, $J = 5 - 4$ emission integrated over the spectral line. Contour interval 2589 K km s⁻¹. The 30 mas convolving beam FWHM for the 43 GHz continuum image is indicated in blue filled circle. The FWHM beams for the H₂O emission of 0.05×0.03 arcsec in PA 65°, and for the SiO $v = 0$, $J = 5 - 4$, 0.05×0.04 arcsec in PA 73°, are shown as the open ellipses in the lower right. The black crosses indicate the centroid positions of the $v = 1$, $J = 2 - 1$ SiO masers mapped by Issaoun et al. (2017).

by the black crosses which lie along the ridges of the peak H₂O emission. H₂O peaks closer to the disk, and SiO extends farther into the lobes. The SiO $v = 0$, $J = 5 - 4$ distribution is similar to that of the SiO $v = 2$, $J = 10 - 9$ mapped by Kim et al. (2019). Kim et al. (2019) also mapped the ²⁹SiO $v=2$ $J=11-10$ and SiO $v=4$ $J=11-10$ lines. The spatial and velocity distribution of these high excitation lines also suggest that they are associated with the base of the outflow at the surface of the disk.

These distributions fit into a scenario where the SiO is formed from grain destruction fol-

lowing the dissociation of H₂O (Schilke et al. 1997). In these models, grain mantles and grain cores are destroyed in shocks; Si is released into the gas phase, and then oxidized by dissociation products of H₂O. In the Src I disk Si can be ablated from disrupted grains by shock velocities >25 km s⁻¹. In the post shock gas, H₂O is depleted onto grains and converted to OH. OH reacts with Si to form SiO, and SiO₂ if OH is abundant. Cohen et al. (2006) note the absence of OH masers within 1300 AU of SrcI where SiO is prominent. OH masers occur in densities $n_{H_2} \sim 10^7$ cm⁻³, close to a shock front where the OH abundance is high. Gain path lengths 1 - 10 AU, not necessarily contiguous, suffice to produce OH masers (Gray et al. 1992), so either chemistry or maser excitation is responsible for their absence closer to SrcI. Greenhill et al. (2013) suggest that shocks from a magnetocentrifugal wind from SrcI, can inject energy further out in the outflow where the outflow speed exceeds the Alfvén and sound speeds. SiO emission extends from the surface of SrcI into the extended outflow lobes, and rotates with SrcI. SiO is a good tracer of shocks. The implication is that the OH is depleted in the inner regions where there is free Si. Our data suggest that chemistry and shock excitation play a significant role in determining these molecular distributions.

4.4. SiS

Figure 11, Figure 12, and Figure 13, show three-color images of the 217.817 GHz SiS line. These color images clearly show the wide-angle bipolar wind from Src I. This feature in SiS is highly limb-brightened. In addition to motion away from Src I with the blueshifted lobe extending NE and redshifted lobe extending SW, the SiS outflow exhibits rapid expansion away from the outflow axis. The SiS outflow is highly asymmetric with a stubby NE blue lobe and a much longer SW red lobe. Weak emission can be traced to the lower-right edge of the figures

above. Also note the patch of SiS emission near the SW corner of the image at the "core" velocities.

Figure 14 compares the 217.817 GHz SiS line with SiO and H₂O emission in 2 km s⁻¹ velocity channels. Like SiO and H₂O, SiS shows rotation close to SrcI. Approximately 50 AU above and below the SrcI disk, close to the maximum extent of the H₂O emission region, the SiO column expands abruptly into a turbulent wide angle outflow. Filaments of SiS emission are particularly prominent along the edges of the outflow.

The distributions of SiO and SiS are consistent with the model of Podio et al. (2017), who argue that SiO results from dust grain destruction, whereas SiS is the product of gas phase chemistry. SiO and SiS are also seen in L1157-B1 in the outflow from this low mass protostar (Podio et al. 2017). As in Orion, SiO and SiS have different spatial distributions: SiO is seen where the molecular jet impacts the outflow cavity wall, but SiS is detected only at the leading edge of the outflow. Zanchet et al. (2018) also considered silicon, oxygen, and sulfur chemistry in postshock gas in protostellar outflows. They found that the main SiS-forming reactions are Si + SO and Si + SO₂, and that SiS is efficiently destroyed through reaction with atomic oxygen.

4.5. SO and SO₂

Figure 15 shows the SO emission at 344.31 GHz, and SO₂ at 334.67 GHz in 2 km s⁻¹ velocity channels. Both SO and SO₂ are heavily absorbed across SrcI at velocities of -8 to +4 km s⁻¹. This is consistent with the 0.2" resolution spectra of SrcI plotted by Plambeck & Wright (2016), in which sulfur-bearing species, including CS and H₂S as well as SO and SO₂, exhibit prominent blueshifted absorption profiles. Since the velocity width of the absorption is comparable with the halfwidth of the SiO emission lines, it is likely that the absorbing molecules are located in the (cooler) outer layers of the SrcI outflow, rather than in unrelated

foreground gas. Examining Figure 15, one sees that SO emission (gray scale) follows the rotation of the outflow close to the disk, while SO₂ does not show this small scale structure. Models of C-type shocks with velocities 5-40 km/s and densities 10⁴ – 10⁶ cm⁻³ can enhance SO and SO₂ abundances by 2 orders of magnitude. SO decreases quickly after the passage of a shock, whilst SO₂ is enhanced during and for some time after the shock (Pineau des Forets et al. 1993).

The SO and SO₂ distributions are over-resolved in these ALMA observations. At lower resolution, SO and SO₂ are seen as a shell of expanding gas, with enhanced abundances where the outflow from SrcI impacts dense clumps around the edges of the outflow (Wright et al. 1996; Wright & Plambeck 2017). Goddi et al. (2011a) suggested that the hot core is excited by the SrcI outflow impacting a dense core. The correspondence of these continuum clumps with the edge of the outflow is shown in Figure 16.

4.6. Unidentified line emission along outflow axis

Figure 16 also shows an unidentified line that appears in two lobes along the outflow axis, centered on SrcI. Assuming the line is centered at 5 km s⁻¹, like the SiO, the rest frequency of the U-line is 354.4945 GHz. Gaussian fits to the spectra at the 2 peaks give velocities 4.3 +/- 0.1, FWHM 5.8 +/- 0.2 km/s for the NE peak, and +5.7 +/- 0.1 km/s, FWHM 6.7 +/- 0.2 km/s for the SW peak.

The U-line is blueshifted to NE like the SiO outflow, but the FWHM is smaller, and the emission is more confined along the outflow axis. There is a vibrationally excited HCN line at 354.4604 GHz ~26 km/s from the U-line centered on 354.4945 GHz in this image. The U-line image has well defined spectral peaks, and has low sidelobes and is probably therefore quite compact, whereas the image of the HCN line emission has large sidelobes suggesting missing larger scale structure. The U-line

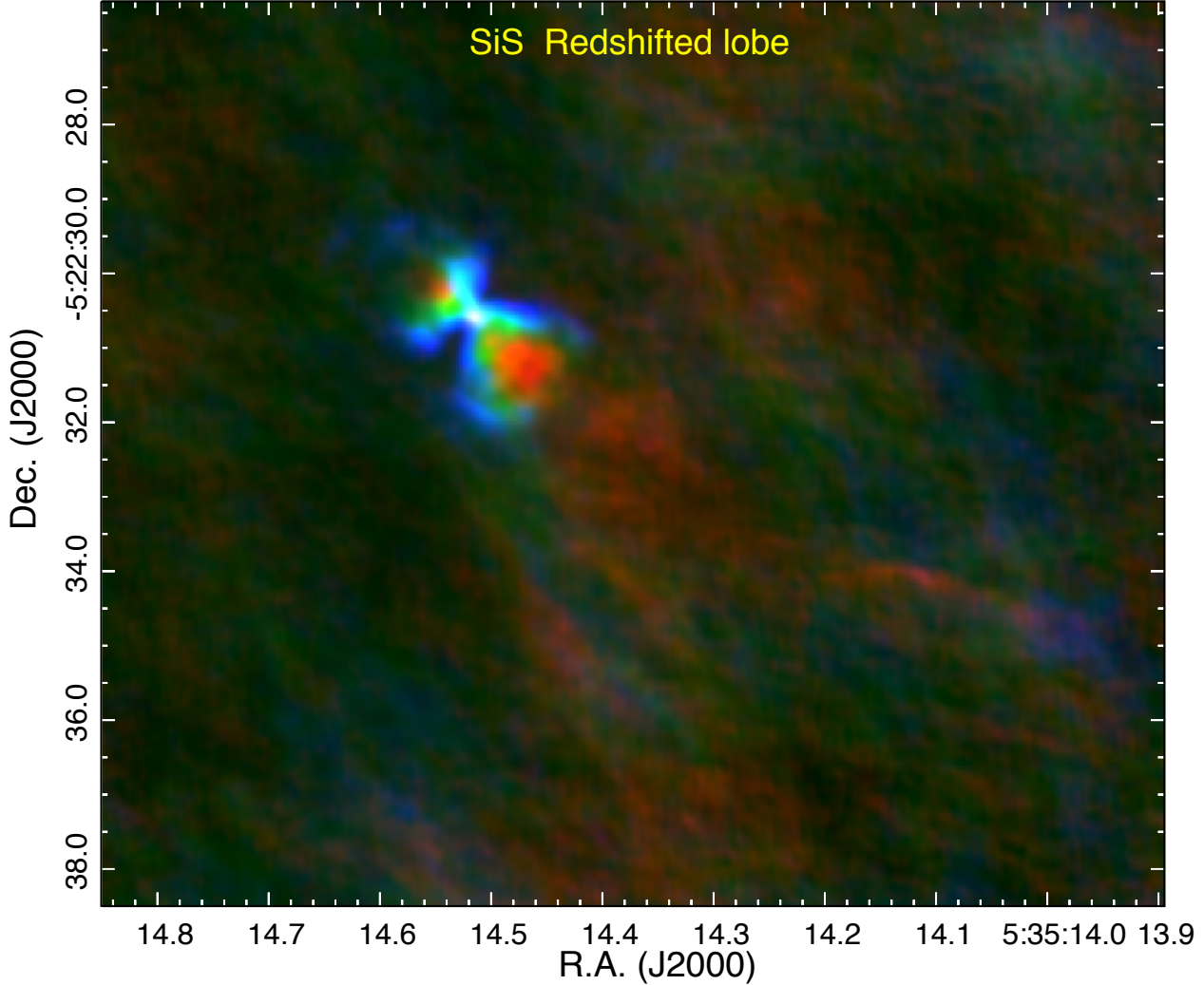


Figure 11. Three-color image of SiS (217.81766 GHz) emission. Blue +4 to +8 km/s, Green +9 to +16 km/s, Red +17 to +30 km/s. The velocity ranges are chosen to highlight the enhancement of SiS emission around the SrcI outflow in the redshifted lobe.

could be an SiO isotopologue or a high vibrational transition illuminated by the central source. The Lovas catalog lists an unidentified line at 354.4968 GHz. In the CDMS catalog there are many lines from 354.49 to 354.50 GHz. Most of them are organic molecules except TiO_2 at 354.4977 GHz, but it is also not convincing.

5. DISCUSSION AND CONCLUSIONS

Our analysis has focused on understanding whether the chemistry seen in SrcI is a result of an “anomalous” history of interactions with its environment, or whether it is directly at-

tributable to the physical conditions of SrcI and its associated outflow, making SrcI a paradigm for the study of high-mass star formation.

The distributions of H_2O , SiO, AlO, and SiS lend strong support to a model in which dust grains are ablated and destroyed close to the disk surface, producing an oxygen rich outflow. The strong SiO maser emission, and AlO mapped in the outflow close to the disk, suggest that refractory grain cores as well as the grain mantles are destroyed. [Lenzuni et al. \(1995\)](#) investigated the evaporation of dust grains in protostellar cores. Carbon grains are destroyed

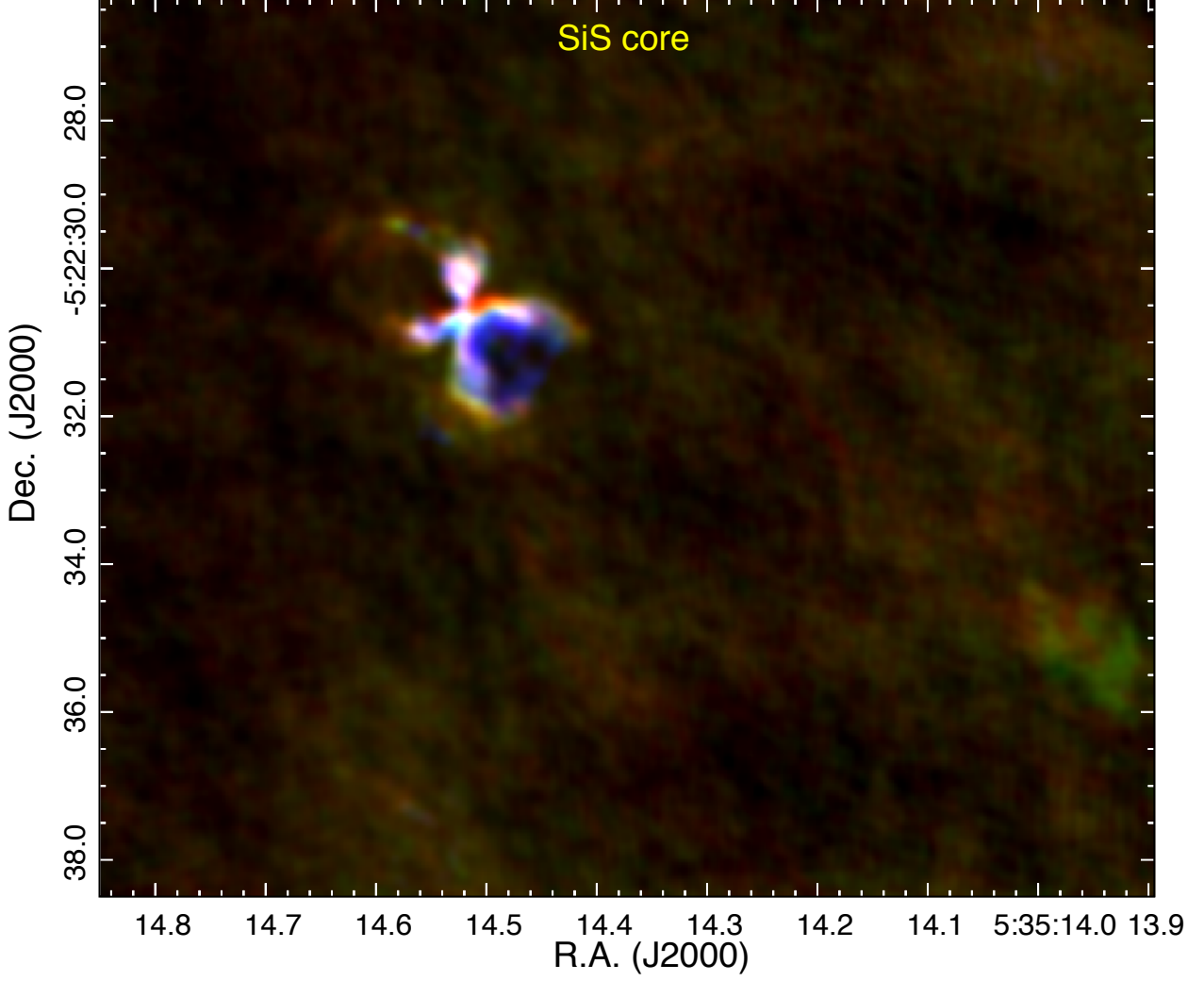


Figure 12. Three-color image of SiS (217.81766 GHz) emission. Blue -3 to -1 km/s, Green 0 km/s, Red +1 to +3 km/s. The velocity ranges are chosen to highlight the enhancement of SiS emission around the SrcI outflow in the SiS core.

Table 1. Observations

freq (GHz)	project code	date	time (min)	synth beam (milliarcsec)	baseline (meters)
43	VLA/18A-136	2018-03-06	291	56×44 at PA 33	500 - 36600
99	2017.1.00497.S	2017-10-12	158	45×36 at PA 47	40 - 16200
216-220	2013.1.005446.S	2014-12 to 2015-04	15	1500×930 at PA -8	14 - 330
224	2016.1.00165.S	2017-09-19	44	39×19 at PA 66	40 - 10500
340	2016.1.00165.S	2017-11-08	45	26×11 at PA 58	90 - 12900
350	2012.1.00123.S	2014-07-26	24	276×260 at PA 85	30 - 730

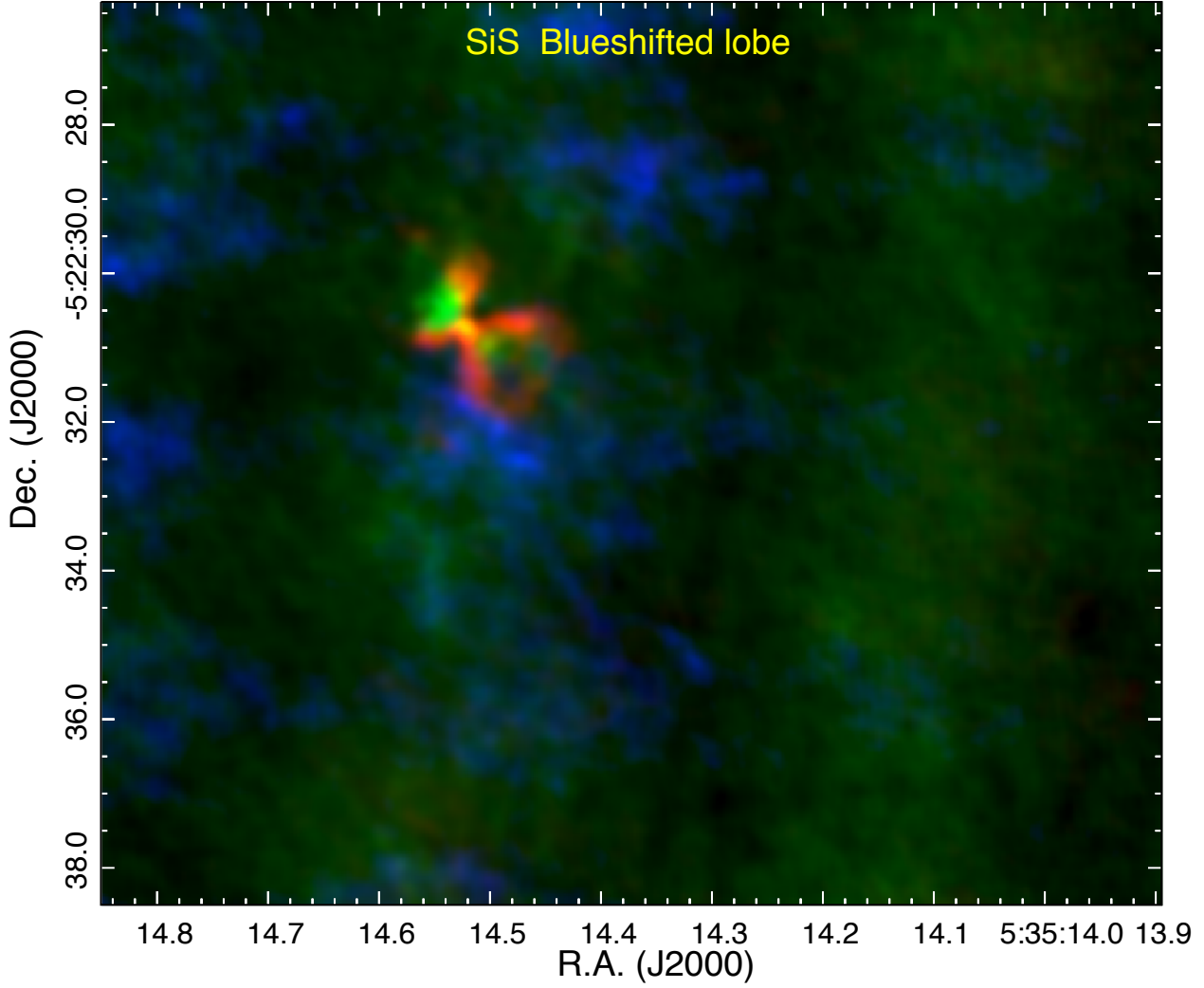


Figure 13. Three-color image of SiS (217.81766 GHz) emission. Blue -23 to -12 km/s, Green -11 to -7 km/s, Red -6 to -3 km/s. The velocity ranges are chosen to highlight the enhancement of SiS emission around the SrcI outflow in the blueshifted lobe.

Table 2. Measured sizes and flux densities for source I

freq (GHz)	beam (arcsec, PA)	deconvolved size (arcsec, PA)	integrated flux (mJy)
43	$0.06 \times 0.04, 33^\circ$	$0.099 \pm 0.002 \times 0.057 \pm 0.002, -40.4^\circ \pm 2.7^\circ$	10 ± 1
99	$0.04 \times 0.04, 47^\circ$	$0.151 \pm 0.005 \times 0.044 \pm 0.002, -37.8^\circ \pm 1.3^\circ$	58 ± 6
224	$0.04 \times 0.02, 66^\circ$	$0.197 \pm 0.003 \times 0.042 \pm 0.003, -37.3^\circ \pm 0.4^\circ$	256 ± 25
340	$0.03 \times 0.01, 58^\circ$	$0.234 \pm 0.005 \times 0.042 \pm 0.002, -37.4^\circ \pm 0.3^\circ$	630 ± 63

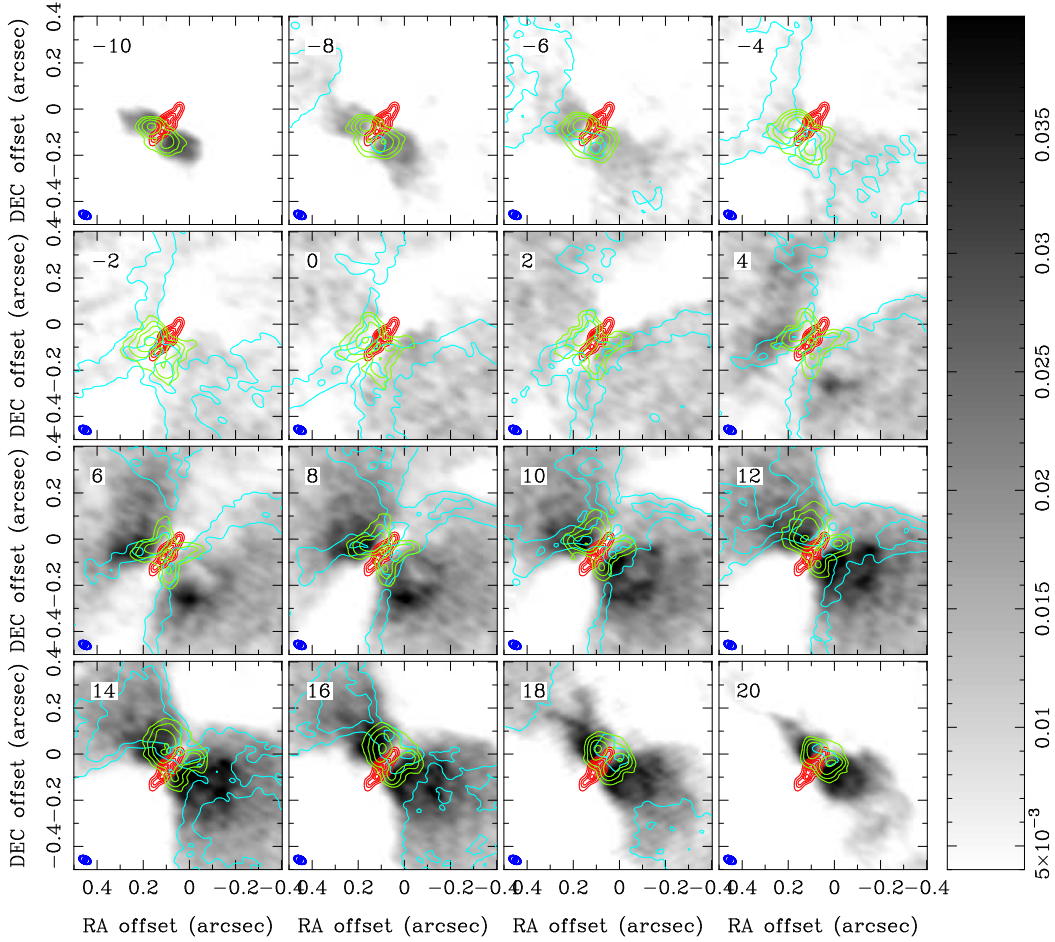


Figure 14. Grey scale shows SiO (217.10498 GHz) in 2 km s^{-1} channels and ranges from 4 to 40 mJy beam^{-1} . Red contours show 99 GHz continuum with contour levels of 1, 2, 3, 4, 5, 6, 7, and 8 mJy beam^{-1} in a 30 mas beam. Blue contours show SiS (217.81766 GHz) in 2 km s^{-1} channels, with contour levels at 100, 200, and 400 K in a $50 \times 30 \text{ mas}$ beam. Green contours show H_2O (232.6867 GHz) in 2 km s^{-1} channels, with contour levels at 100, 200, and 400 K in a $50 \times 30 \text{ mas}$ beam. The convolving beams is indicated in blue in the lower left.

at temperatures $\sim 800 - 1150 \text{ K}$. Silicate grains are evaporated at temperatures $\sim 1300 \text{ K}$, followed by AlO at $\sim 1700 \text{ K}$. SiO and AlO may be released directly from the grains, or may be formed in the gas phase by the oxidation of Si and Al. Thermal emission from the ground state, $v = 0$, SiO traces a turbulent, wide angle outflow extending over 1000 AU from a position close to the maximum extent of the H_2O emission from the disk (Plambeck et al. 2009). SiS traces a more filamentary structure which is prominent at edges of extended SiO outflow. Zanchet et al. (2018), in a study of silicon, oxygen, and sulfur chemistry, found that the main

formation for SiS are from SO and SO_2 which are seen as a shell around the edges of the outflow (Wright et al. 1996).

One might ask if the chemistry of the bipolar outflow is distinct from that of the larger “finger system” produced by the BN-SrcI explosive event. The finger system is over an arcminute in extent, and so is almost completely resolved out in our high resolution images. CO emission from the fingers was mapped by Bally et al. (2017) with approximately $1''$ resolution using mosaic observations with ALMA. Those data also cover transitions of SiO ($J=5-4 \text{ } v=0$; 217.105 GHz), SO (219.95 GHz), and

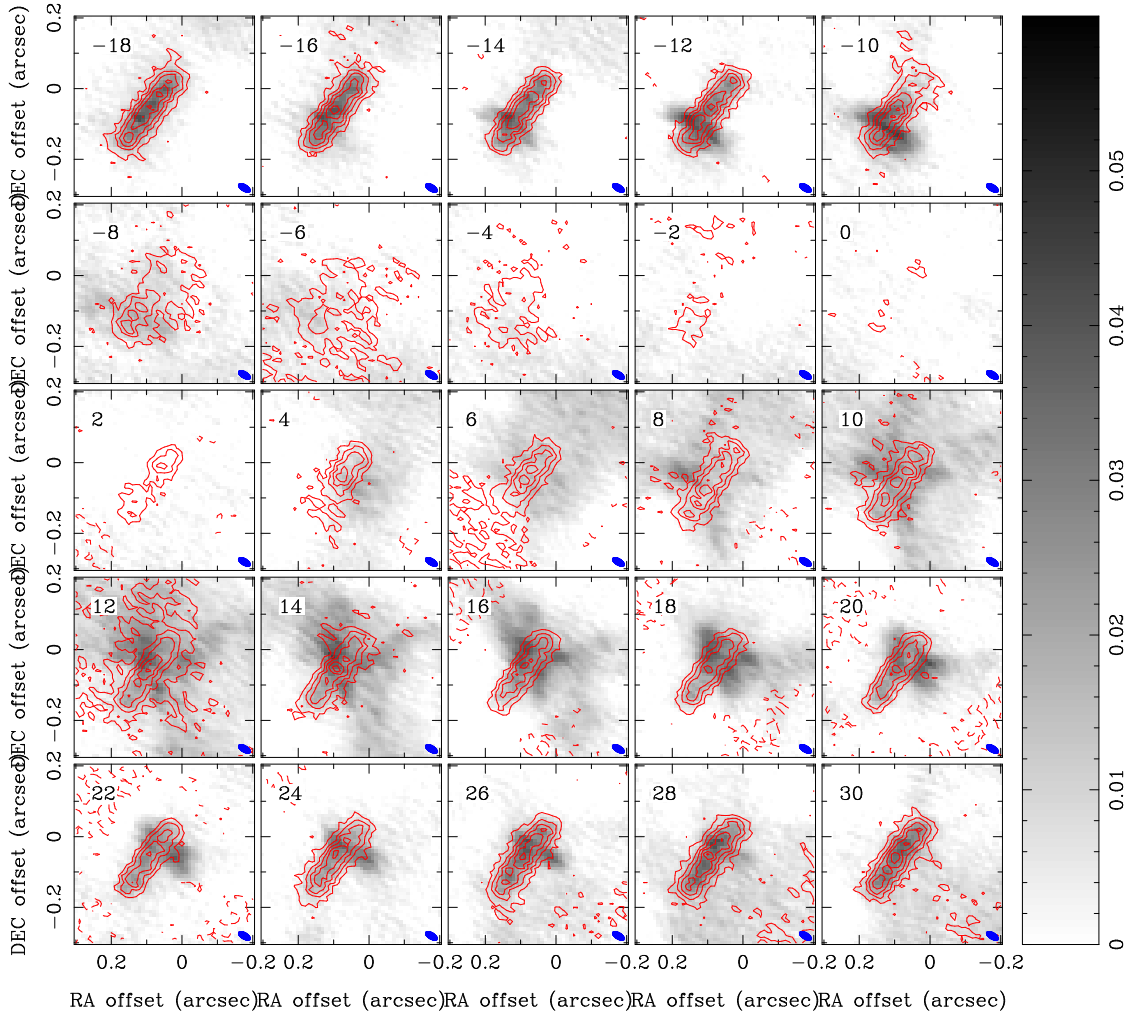


Figure 15. SO and SO₂ emission and absorption across SrcI. Both images plot line emission + continuum emission from the disk to show the line absorption across the disk. The grey scale image shows the SO at 344.31 GHz. Peak 0.039 Jy/beam = 655 K. The contours show the SO₂ at 334.67 GHz. Contour interval 129 K, peak 729 K. The convolving beam 36×17 mas FWHM in PA = 59 deg is indicated in blue in the lower right.

SO₂ (216.64 GHz). We used the mosaic ALMA data to generate 2 km s^{-1} channel maps of these three molecular lines over a $30''$ region centered on SrcI. These images are compared in Figure 17. Both the SiO and SO images exhibit streamers similar those seen in CO; the situation for SO₂ is less clear. The SiO fingers east of SrcI at velocities $>30 \text{ km s}^{-1}$ were noted earlier by Plambeck et al. (2009) (see their Figure 4). It is extremely difficult to distinguish the outflow from the finger system in any of these images. In these molecular lines, at least, there appear to be no clear chemical or excitation differences

between the bipolar outflow and the explosive event.

It is possible that the SrcI/BN interaction, resulting in a collapse of a binary protostar in SrcI, and the disruption of the disk around SrcI, dredged up the inner part of the disk, and made oxygen and sulfur rich material available for both the SrcI outflow and the explosion, and moved dust grains containing refractory material like AlO and salts to the outer parts of the disk where they could be ablated by the SrcI outflow. The energy for the ejection of SrcI and BN, and the explosion in the gas must have

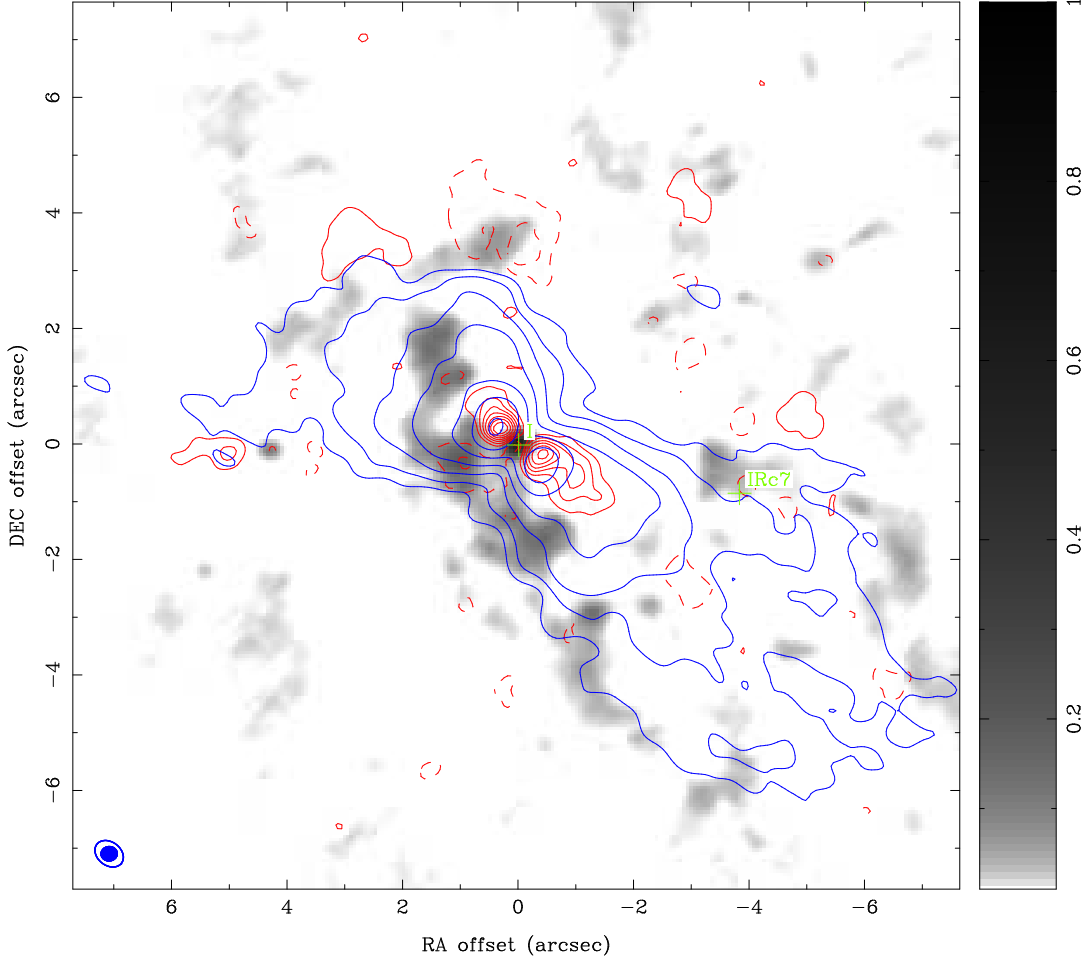


Figure 16. Continuum emission around the edges of the SiO J=2-1 $v=0$ line (Blue contour levels 0.05 0.1 0.2 0.4 0.8 1.6 3.2 Jy/beam (746 K/Jy), integrated over -10 to + 20 km/s). Red contours map the integrated emission over 11 km/s from an unidentified line at 354.4945 GHz. Contour interval 14.8 K. The grey scale image shows the continuum emission at 348 GHz (141 K/Jy). The convolving beams, $0.28 \times 0.26''$ for the unidentified line and continuum emission, and $0.54 \times 0.41''$ for the SiO are indicated in blue in the lower left.

come from gravitational binding energy exceeding 10^{48} ergs (Bally et al. 2017). The violence of the interaction ~ 550 years ago would have strongly shocked the disk, resulting in chemistry. The AIO and salts could be a bi-product of this interaction. As the disk relaxed from its perturbed state, it could have triggered a major accretion event onto the central binary or a merger which produced the current Src I outflow with about the same age. At 50 AU, the disk is well inside the Src I gravitational radius for a 10 km s^{-1} ejection speed. Thus the disk is likely made of material that was already bound

to one of more stars involved in the interaction - no need for Bondi-Hoyle accretion over the last 500 years. Moeckel & Goddi (2012) studied the chances of disk survival in binary-single stellar interactions with N-body simulations.

Observations of other high mass protostar outflows are required to see if H_2O , sulfur and Si molecules, and salts are common or if the SrcI outflow is unusual. We adopt as a working hypothesis, that the rich chemistry seen in SrcI is a direct consequence of the outflow from a high mass protostar and does not depend on the particular environment and history of SrcI.

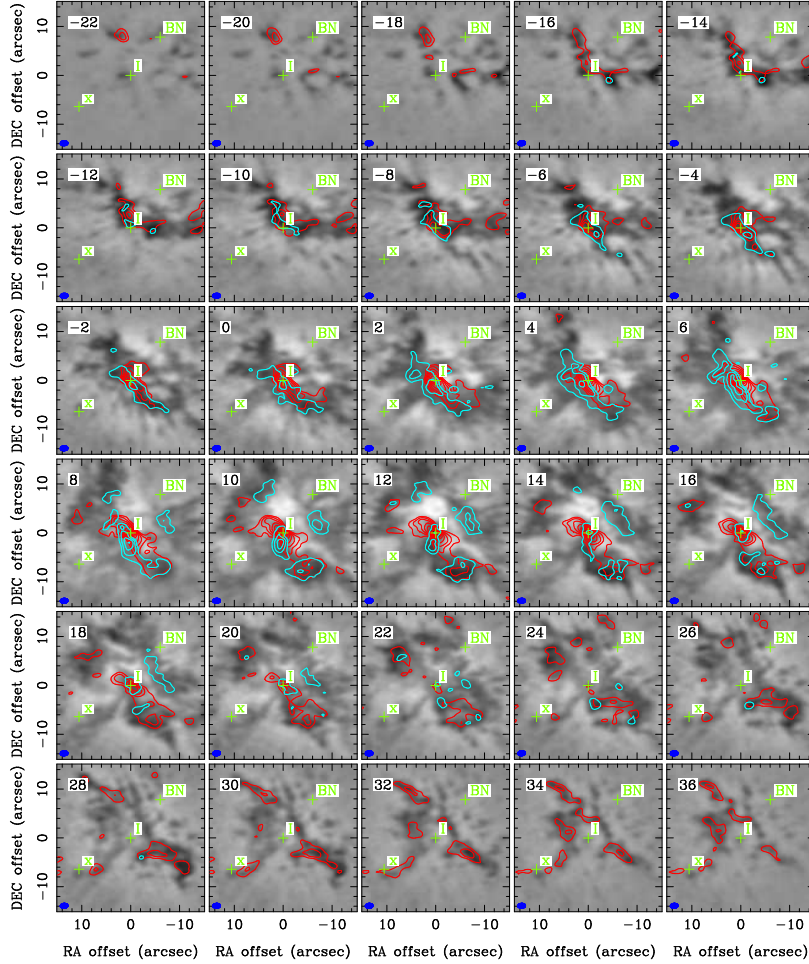


Figure 17. SiO, SO and SO₂ emission associated with the explosion resulting from the SrcI/BN interaction. The gray scale image shows the SO at 219.95 GHz. The extended SO emission is heavily resolved in these ALMA observations, but nicely shows the filamentary structure. The gray scale range is -65 to +85 K. The red contours show the SiO emission at 217.10 GHz, and the blue contours show the SO₂ emission at 216.64 GHz. The contour interval is 19 K in both SiO and SO₂. The convolving beam FWHM of 1.5'' × 0.9'' is indicated in blue in the lower left.

If, indeed, Orion SrcI, as the closest and best studied example of a young high mass protostar, is a paradigm model, then future observations of other high-mass star formation regions will have many tools available. The resolution and sensitivity of our ALMA observations are sufficient to detect disks and outflows similar to those seen in SrcI out to ~ 2 kpc. Our ~ 50 mas resolution images (100 AU at 2 kpc) have an RMS brightness sensitivity ~ 10 K at 2 km s^{-1} velocity resolution which would be sufficient to detect and image SiO, SiS, H₂O, and salt distri-

butions in outflows from putative disks around other high mass protostars.

Our observations from 43 to 350 GHz allow us to map the dust opacity at the surface of the disk around SrcI. NaCl and KCl trace the rotation of the surface layers of SrcI, allowing us to estimate the mass of the protostar. Salt emission is confined to the dust layer where there is a large spectral index gradient. NaCl excitation temperatures estimated from rotational transitions over a large range of frequencies could be underestimated because of greater dust opacity at high frequencies, whereas the vibrational

temperatures, estimated over a small range of frequencies, are less affected.

H₂O emission maps the distribution of material released from grain mantles. SiO maps the more extended outflow. Maps of SiS and SO in other outflows could support the role of gas phase chemistry in the post shock gas in the outflow.

This paper makes use of the following ALMA data: ADS/JAO.ALMA#2012.1.00123.S, ADS/JAO.ALMA#2013.1.00546.S, ADS/JAO.ALMA#2016.1.00165.S, ADS/JAO.ALMA#2017.1.00497.S. ALMA is a partnership of ESO (representing its member states), NSF (USA) and NINS (Japan), together with NRC(Canada) and NSC

and ASIAA (Taiwan), in cooperation with the Republic of Chile. The Joint ALMA Observatory is operated by ESO, AUI/NRAO and NAOJ.

The National Radio Astronomy Observatory is a facility of the National Science Foundation operated under cooperative agreement by Associated Universities, Inc. TH is financially supported by the MEXT/JSPS KAKENHI Grant Numbers 24684011, 17K05398 and 18H05222. We thank the referee, Paul Ho, for a careful reading which has improved the presentation of this paper.

Facilities: ALMA, JVLA

Software: Miriad (Sault et al. 1995)

REFERENCES

- Bally, J., Ginsburg, A., Arce, H., et al. 2017, ApJ, 837, 60
- Cohen, R. J., Gasiprongs, N., Meaburn, J., & Graham, M. F. 2006, MNRAS, 367, 541
- Ginsburg, A., Bally, J., Goddi, C., Plambeck, R., & Wright, M. 2018, ApJ, 860, 119
- Ginsburg, A., McGuire, B., Plambeck, R., et al. 2019, The Astrophysical Journal, 872, 54.
<https://doi.org/10.3847/2F1538-4357%2Faafb71>
- Goddi, C., Greenhill, L. J., Chandler, C. J., et al. 2009, ApJ, 698, 1165
- Goddi, C., Greenhill, L. J., Humphreys, E. M. L., Chandler, C. J., & Matthews, L. D. 2011a, ApJL, 739, L13
- Goddi, C., Humphreys, E. M. L., Greenhill, L. J., Chandler, C. J., & Matthews, L. D. 2011b, ApJ, 728, 15
- Gómez, L., Rodríguez, L. F., Loinard, L., et al. 2008, ApJ, 685, 333
- Gray, M. D., Field, D., & Doel, R. C. 1992, A&A, 262, 555
- Greenhill, L. J., Goddi, C., Chandler, C. J., Matthews, L. D., & Humphreys, E. M. L. 2013, ApJL, 770, L32
- Hirota, T., Kim, M. K., Kurono, Y., & Honma, M. 2014, ApJL, 782, L28
- Hirota, T., Machida, M. N., Matsushita, Y., et al. 2017, Nature Astronomy, 1, 0146
- Issaoun, S., Goddi, C., Matthews, L. D., et al. 2017, A&A, 606, A126
- Kim, M. K., Hirota, T., Machida, M. N., et al. 2019, ApJ, 872, 64
- Kim, M. K., Hirota, T., Honma, M., et al. 2008, PASJ, 60, 991
- Kounkel, M., Covey, K., Suárez, Genaro a nd Román-Zúñiga, C., et al. 2018, AJ, 156, 84
- Lenzuni, P., Gail, H.-P., & Henning, T. 1995, ApJ, 447, 848
- Matthews, L. D., Greenhill, L. J., Goddi, C., et al. 2010, ApJ, 708, 80
- Menten, K. M., Reid, M. J., Forbrich, J., & Brunthaler, A. 2007, A&A, 474, 515
- Moeckel, N., & Goddi, C. 2012, MNRAS, 419, 1390
- Niederhofer, F., Humphreys, E. M. L., & Goddi, C. 2012, A&A, 548, A69
- Pineau des Forets, G., Roueff, E., Schilke, P., & Flower, D. R. 1993, MNRAS, 262, 915
- Plambeck, R. L., & Wright, M. C. H. 2016, ApJ, 833, 219
- Plambeck, R. L., Wright, M. C. H., Friedel, D. N., et al. 2009, ApJL, 704, L25

- Podio, L., Codella, C., Lefloch, B., et al. 2017, Monthly Notices of the Royal Astronomical Society: Letters, 470, L16
- Reid, M. J., Menten, K. M., Greenhill, L. J., & Chandler, C. J. 2007, ApJ, 664, 950
- Rodríguez, L. F., Poveda, A., Lizano, S., & Allen, C. 2005, ApJL, 627, L65
- Sault, R. J., Teuben, P. J., & Wright, M. C. H. 1995, in ASP Conf. Ser. 77: Astronomical Data Analysis Software and Systems IV, Vol. 4, 433. http://adsabs.harvard.edu/cgi-bin/nph-bib_query?bibcode=1995adass...4..433S&db_key=AST
- Schilke, P., Walmsley, C. M., Pineau des Forets, G., & Flower, D. R. 1997, A&A, 321, 293
- Tachibana, S., Kamizuka, T., Hirota, T., et al. 2019, The Astrophysical Journal, 875, L29. <https://doi.org/10.3847%2F2041-8213%2Fab1653>
- Vaidya, B., & Goddi, C. 2013, MNRAS, 429, L50
- Wright, M. C. H., & Plambeck, R. L. 2017, The Astrophysical Journal, 843, 83
- Wright, M. C. H., Plambeck, R. L., & Wilner, D. J. 1996, ApJ, 469, 216
- Zanchet, A., Roncero, O., Agúndez, M., & Cernicharo, J. 2018, ApJ, 862, 38